INTERNATIONAL JOURNAL FOR NUMERICAL METHODS IN ENGINEERING
Int. J. Numer. Meth. Engng 0000; **00**:1–20
Published online in Wiley Online Library (www.onlinelibrary.wiley.com). DOI: 10.1002/nme.5786

An adaptive cracking particle method providing explicit and accurate description of 3D crack surfaces

Weilong Ai*and Charles E. Augarde

Department of Engineering, Durham University, South Road, Durham, DH1 3LE, UK

SUMMARY

Cracks in 3D have arbitrary shapes and therefore present difficulties for numerical modelling. A novel adaptive cracking particle method with explicit and accurate description of 3D cracks is described in this paper. In this meshless method, crack surfaces are described by a set of discontinuous segments which are associated with particles. This group of particles are assumed all to be "cracked" and split into two sub-particles with modified support domains. Compared to the original method where the spherical supports at particles are equally divided, the proposed method makes use of non-planar segments to account for changes in crack face direction. The orientations of those segments and the angular changes of cracks during crack propagation steps are recorded using triangular meshes. Supports of weight functions are modified according to those changes so that quasi-continuous crack surfaces can be obtained, avoiding the spurious cracking seen in earlier CPMs. An adaptive approach in 3D is then introduced to capture stress gradients around crack fronts. Several 3D crack problems with reference results have been tested to validate the proposed method with good agreement being achieved using the new method, showing it to be potentially a significant advance for 3D fracture predictions problems. Copyright © 0000 John Wiley & Sons, Ltd.

Received . . .

KEY WORDS: Cracking particles, meshless, 3D cracks, Adaptive

1. INTRODUCTION.

Crack modelling in 3D is a challenging problem in computational fracture mechanics. The majority of the literature, as reviewed in [1, 2], to date on computational fracture mechanics focuses on 2D problems with assumptions of plane strain or plane stress to reduce complexity and for ease of comparison with analytical solutions. However, for any of these methods to be of real industrial use, robust 3D formulations are needed.

The standard finite element method (FEM), being the most popular numerical method for solid mechanics, has the longest history of being applied to 3D crack modelling [3], where crack surfaces are described by element interfaces. Cracks are forced to propagate along element faces and elements are remeshed to align element shapes to crack patterns. The dependence of crack modelling on remeshing is removed by adding enrichment functions in the polynomial approximation space,

*Correspondence to: Weilong Ai, Department of Engineering, Durham University, South Road, Durham, DH1 3LE, UK.Email: weilong.ai@durham.ac.uk

as in the extended finite element method (XFEM) [4, 5, 6, 7], where cracks can be arbitrary shapes and remeshing is not required. Various authors have developed the XFEM where crack surfaces in 3D are represented by a set of triangles [8] or by level set functions [9]. The former can provide explicit descriptions of crack geometries but crack surfaces are not smooth. Crack modelling by the latter can be more accurate, but updating those level set functions is not computationally cheap, as mentioned in [10, 11]. A hybrid of the two is given in [12] to make use of the advantages of both methods. Another approach is the numerical manifold method (NMM) [13, 14], which originates from the differential manifold approach [15]. Cracks are introduced by dividing physical covers, used to define weight functions into small elements, and interpolation approximations based on those elements are discontinuous. This approach has also been applied to 3D crack propagation simulation in [16] but is challenging for cover generation for complex cracks as mentioned in [17].

Mesh-based methods for computational fracture often bring problems of remeshing, mesh distortion and volumetric locking [18]. Meshless methods use only node data to discretize a problem domain and those issues are usually avoided. Meshless methods usually have high order continuous shape functions rather than the C^0 continuous shape functions in the standard FEM, which can help to capture the stress gradients around crack tips. In meshless methods, the element free Galerkin method (EFGM) has shown its ability to handle problems involving static cracks [19, 20, 21] and dynamic fracture [22, 23, 24], and the extension to 3D problems has been demonstrated to be straightforward [25, 26, 27]. Crack discontinuities are introduced by modifying basis functions [28] or weight functions [29, 30]. An advantage over the XFEM is that high stress gradients can be obtained without asymptotic enrichments [28], or by using special weight functions at crack fronts [27]. However, tracking the crack geometries in 3D fracture modelling remains challenging for meshless methods and approaches have included using a triangular mesh [26, 27, 30], or level set functions [29]. An alternative to methods like the EFGM is peridynamics, where crack discontinuities are obtained by removing "bonds" between nodes [31]. It is not difficult for this method to handle multiple cracks and crack branching [32] as compared with the XFEM using enrichment functions, and an application to 3D cracks is in [33], although much work is needed to bring this method to maturity for a useful range of materials. Another alternative meshless approach is the cracking particle method (CPM) [34], where crack paths/faces are described by a set of discontinuous segments centred at cracking particles. Since the locations and orientations of these segments are arbitrary, it is suitable for complex fracture problems [35, 36, 37, 38], and applications for 3D crack problems can already be found in [39, 40], although some of the early CPMs [40, 41] were shown to predict spurious cracking patterns, which have been relieved by employing modifications [42]. In the modified 2D CPM in [42], supports of weight functions are modified through bilinear segments with consideration of cracking angle changes at particles rather than straight segments as in [34]. This allows crack kinks and branches inside a particle and removes issues with spurious cracking. This idea is extended here to 3D crack problems where a framework including explicit crack description has now been developed. Triangular meshes are introduced in this CPM and the supports of cracking particles are modified accordingly to prevent spurious cracking, leading to more accurate simulation of continuous crack surfaces in 3D. Only linear elastic fracture mechanics (LEFM) is considered in this paper since the key contribution lies in the description of crack geometries in 3D and the adaptive approach, but the extension to cohesive models is not difficult as in [34, 39] and is a topic of ongoing research [43].

The article is arranged as follows: strategies of the original and the modified CPM are described and an adaptive approach is briefly introduced in Section 2. Then, crack modelling in 3D is illustrated and the crack propagation criterion used is included in Section 3. A number of examples are given in the following section to validate the proposed methodology.

2. A MODIFIED CRACKING PARTICLE METHOD FOR LEFM.

The modified and original CPMs are based on the EFGM, for which the governing equations have been included in many papers, e.g. [18, 44] and consequently we do not repeat them here.

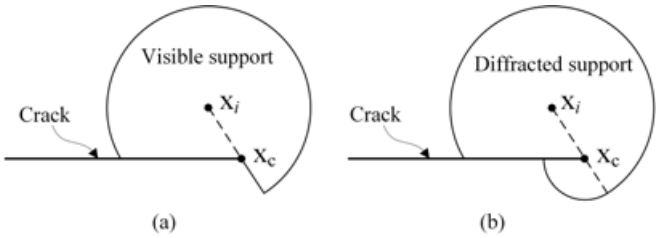

Figure 1. Modification of supports of weight functions: (a) visibility criterion; (b) diffraction criterion

2.1. Modelling of crack discontinuities.

A key issue in computational fracture mechanics is modelling the displacement discontinuity across a crack. In methods that do not explicitly model crack faces as domain edges, there are principally two ways to enforce these discontinuities: extrinsic enrichment and intrinsic enrichment.

The first of these involves the addition of discontinuous terms in the expression of approximated displacements $u^h(\mathbf{x})$ as in the XFEM [4, 45, 5], i.e.

$$u^h(\mathbf{x}) = \sum_i^n \Phi_i(\mathbf{x}) u_i + \sum_i^{n_1} \Phi_i(\mathbf{x}) H(\mathbf{x}) b_i, \tag{1}$$

where $\mathbf{x}$ is the spatial location vector in a problem domain, $\Phi_i(\mathbf{x})$ are shape functions, $H(\mathbf{x})$ are sign functions, u_i are nodal values, b_i are extra unknowns, n is the number of particles with support covering $\mathbf{x}$ and n_1 is the number of displacement enriched particles in n, and here crack tip enrichments are not included. One disadvantage of this approach is that extra unknowns are introduced, therefore leading to higher computational cost, and the approach can also lead to an ill-conditional global stiffness matrix, in that these additional unknowns are not related to physical degrees of freedom.

In comparison, no extra unknowns are added using an intrinsic enrichment. The discontinuities in displacement are simulated by the modification of the influence domain (also known as the support) of weight functions for particles on or adjacent to cracks. A simple way to achieve this is via the *visibility* criterion [18]. The support of an affected particle's weight function is truncated by the crack line as in Fig 1 (a) and discontinuities at cracks are therefore constructed. But there is a sudden change of active shape functions on the truncation line, and oscillations can occur in the solutions for displacement around the crack tip especially when large support sizes are used [46]. In an alternative approach, the *diffraction* criterion, a small zone around the crack tip is included (Fig 1 (b)), and the input parameter of the weight function is modified accordingly as in [46]. A comparison of the two methods is described in [47], in which the diffraction criterion shows better accuracy around the crack tip. However, the diffraction criterion approach requires locating the nearest crack front, which can become computationally expensive in 3D [27].

2.2. The development of the CPM.

In the original CPM described in [34], discontinuities are introduced by using extrinsic enrichments, borrowing ideas from the XFEM, with displacement approximations similar to Eq (1). The main difference is that here a continuous crack path is approximated by a group of discrete segments which are centred at particles and used to define the discontinuities of those particles' weight functions, as shown in Fig 2. The method has been applied to brittle fracture [35], ductile fracture [37] and dynamic cracks [36] and is extended to 3D cracks in [39].

The extra unknowns associated with the enrichment are removed as a development of the original CPM in [40] with the use of intrinsic enrichment. Cracking particles are split into two parts and supports of weight functions are divided equally. The crack opening magnitudes are evaluated by

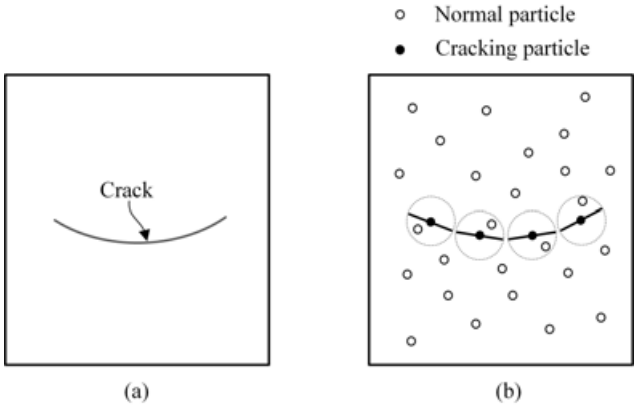

Figure 2. Crack path described by the cracking particle method: (a) practical path; (b) approximation.

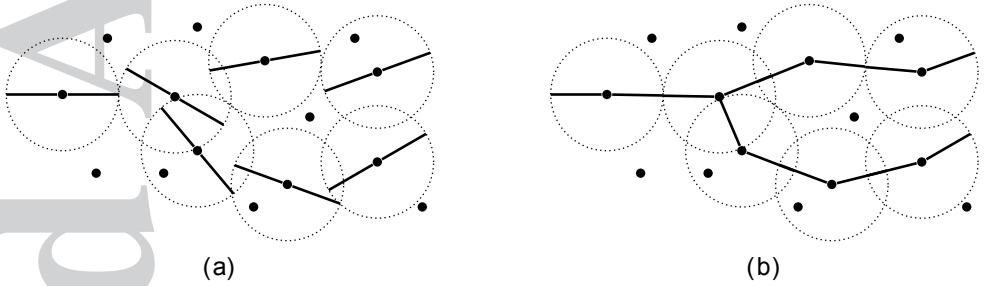

Figure 3. Comparison between the original and the modified CPM: (a) original CPM; (b) modified CPM.

tracking relative displacements of pairs of cracking particles,

$$[\![u(\mathbf{x})]\!] = \sum_{i \in S^+} \Phi_i(\mathbf{x}^{S^+}) u_i - \sum_{i \in S^-} \Phi_i(\mathbf{x}^{S^-}) u_i, \tag{2}$$

where S^+ and S^- indicate the two sides of the crack.

In the original 2D CPM, cracking particles are defined as each carrying a straight discontinuous segment of the crack face, splitting the supports as in Fig 3 (a). If there is a "bad" overlap between segments, spurious cracking occurs. The current authors have presented a modified strategy for 2D in [42] to solve this problem by using bilinear segments where the crack path can change direction at each cracked particle. All discontinuous segments are aligned and "good" overlaps are obtained, as in Fig 3 (b).

2.3. Adaptivity.

Using any discretised approach, capturing the high stress gradients around crack fronts usually requires a high degree of refinement, and the computational cost can therefore be high for the required accuracy. An adaptive approach allows modelling to start from a coarse discretization which is iteratively refined automatically based on an error indicator or estimator. Error estimators used in adaptive approach for solid mechanics are either recovery [48, 49, 50] or residual-based [51, 52]. An *a posteriori* adaptive approach with an recovery-based error estimator has been developed by the authors for the 2D modified CPM in [42]. The error terms are the difference between calculated stresses $\boldsymbol{\sigma}^h$ and exact stresses $\boldsymbol{\sigma}^e$ using the energy norm [47].

$$\|e\| = \left\{ \frac{1}{2} \int_\Omega (\boldsymbol{\sigma}^e - \boldsymbol{\sigma}^h)^{\mathrm{T}} \boldsymbol{D}^{-1} (\boldsymbol{\sigma}^e - \boldsymbol{\sigma}^h) \mathrm{d}\Omega \right\}^{1/2}, \tag{3}$$

where $\boldsymbol{D}$ is the elastic constitutive matrix, $\boldsymbol{\sigma}^h$ and $\boldsymbol{\sigma}^e$ are vectors of stresses and integration is carried out over a problem domain Ω. Exact stresses $\boldsymbol{\sigma}^e$ are generally unknown and are instead approximated by the "projected" stresses $\boldsymbol{\sigma}^p$ [47],

$$\boldsymbol{\sigma}^e(\mathbf{x}) \approx \boldsymbol{\sigma}^p(\mathbf{x}) = \sum_{k=1}^{m} \Psi_k(\mathbf{x}) \boldsymbol{\sigma}^h(\mathbf{x}_k), \tag{4}$$

where m is the number of surrounding particles with locations $\mathbf{x}_k$ and stresses $\boldsymbol{\sigma}^h(\mathbf{x}_k)$, and $\Psi_k(\mathbf{x})$ are shape functions calculated by the standard moving-least square process where smaller supports are used. The global relative error η is calculated as

$$\eta = \frac{\|e\|}{\|U\|}, \tag{5}$$

where the normalising term

$$\|U\| = \left\{ \frac{1}{2} \int_{\Omega} (\boldsymbol{\sigma}^h)^{\mathrm{T}} \mathbf{D}^{-1} (\boldsymbol{\sigma}^h) \mathrm{d}\Omega \right\}^{1/2}. \tag{6}$$

The local error $\|e_i\|$ in a background cell i (as needed in the EFGM for numerical integration) is estimated using Eq (3) with the problem domain Ω replaced by the area of the cell Ω_i, and the local relative error follows as $\eta_i = \frac{\|e_i\|}{\|U\|/\sqrt{n}}$ where n is the total number of background cells. Background cells with large errors are divided following a quad-tree structure in 2D [50, 42] and an octree structure in 3D [53]. New particles are added at the vertices of the divided cells in the same way as a recent adaptivity approach for peridynamics [54, 55], but a difference lies in the triggers for adaptive refinement. In the proposed method, refinement is applied to background cells with large errors estimated by Eq (3), while the refinement in the peridynamics approach [54, 55] is activated when the density of potential energy exceeds a predefined threshold value. The difference is because the proposed CPM is based on the weak form of governing equations, while peridynamics makes use of the strong form.

3. CRACK MODELLING IN 3D.

Moving from 2D to 3D is challenging, both because it leads to a heavier calculation burden but also brings difficulties due to more complex crack patterns. A contribution to the former arises from the larger matrix requiring inversion for calculation of shape functions at every integration point. For a linear basis in 2D the size of the moment matrix $\mathbf{A}^{-1}$, required in the moving least square process, is 3×3, but in 3D becomes 4×4, as mentioned in [18].

Considering the latter source of complexity, crack paths and fronts in 2D are lines and points respectively, but in 3D become surfaces and curves respectively, and aspects of the formulations become considerably more complex. An example is the use of the visibility criterion. In 2D the check involves locating the intersection point E of the connection of two particles C and D and a crack face AB in Fig 4 (a). If E is within the line AB, then particle C must be outside the support of particle D and therefore they are invisible to each other. For a 3D crack with a curved front, as shown in Fig 4 (b), the line used for checking the visibility is AB which is shorter than AB'. E is outside of the line AB, so particles C and D are visible.

3.1. Crack surfaces in 3D.

Tracking the geometries of 3D cracks is one major challenge. Description of 3D crack surfaces in the literature to date is mostly achieved by one of two methods: triangular meshes [8, 26, 27, 30] and level sets [9, 29], and both make use of so-called "ghost" nodes to capture crack geometries in either the XFEM or the EFGM.

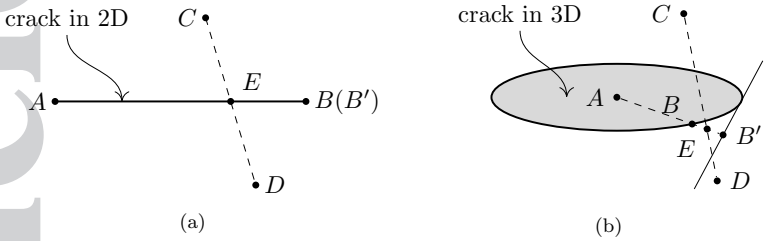

Figure 4. The visibility criterion: (a) 2D crack; (b) 3D crack

Here we describe a new approach using the modified CPM which is related to previous uses of triangular facets but which is capable of handling both static cracks and propagating cracks. At each particle in a 3D crack problem modelled using the original CPM, there is a discontinuous circular plane in its support and the weight function is modified as in Fig 5 (a). The idea of bilinear segments for the 2D modified CPM in [42] is here extended to 3D crack problems and a strategy of non-planar discontinuous segments is now proposed as in Fig 5 (b-d). Crack surfaces are described by a group of cracking particles as before, which are connected by a triangular mesh (Fig 6). The vertices of these triangular elements are the cracking particles. The orientations of the discontinuous segments (the triangular facets) are defined through the locations of the cracking particles: particle a, which is located within a triangle, has a support as in Fig 5 (a); particle b, on an edge in the mesh, has a support as shown in Fig 5 (b); supports of particles c and d, on the vertices, are as shown in Fig 5 (c-d). The information specifying triangular meshes connected to one cracking particle is recorded in a matrix, so the maximum number of facets that can be connected to any one particle is limited and set to eight for simplicity and economy. The particles in black in Fig 6 are crack front particles and are not themselves split, in that the crack front has an influence on the two sides of the crack. The influence domain of a cracking particle close to the crack front is fully truncated, although the crack may not cross the entire influence domain, because this cracking particle does not affect the other side of the crack following the visibility criterion, which is applied to check the connectivity between particles with the triangular mesh representing the crack surface. Since a pair of cracking particles across the crack surface share the same location during this process, cracking particles are given tiny shifts to the two sides of the crack surfaces and then the standard algorithm to check the connectivity between particles operates. The magnitude of the shift is 0.01 of the cracking particle's support size. However, the original locations of cracking particles are used to calculate shape functions. It is notable that other types of meshes can also be used for the description of crack surfaces, especially for cracks with simple geometries. For instance, a penny-shaped crack can be modelled by a circular cell which is the initial crack itself, and triangular meshes are only used to describe the crack propagation, as will be shown later.

Only single cracks in 3D are considered here for simplicity, although the CPM has been applied to non-linear fracture problems including crack branching and crack coalescence [34, 39, 40]. While branched cracks can be modelled with the proposed CPM as in [56], branching itself is not included here as this is a feature of dynamic crack propagation, and an implicit quasi-static code is currently used. An additional criterion is required to determine whether a crack branches, which is not method dependent and obtained through considering the physics of the problem. The further application of the proposed CPM to dynamic fracture is a future plan.

3.2. Calculation of stress intensity factors (SIFs).

After the governing equations are solved, SIFs at crack fronts need to be extracted from the solution. The calculation of SIFs is often achieved via the J-integral [57] following a contour path in 2D or over a volume for 3D. In the contour integral approach in 3D, symmetric and antisymmetric stresses are used to decompose the three modes of SIFs as in [58, 29], but there are extra terms for the energy contribution from the normal direction of the contour plane and the derivatives of stresses are involved [25]. These derivative terms are avoided by transferring the path integral to a volume

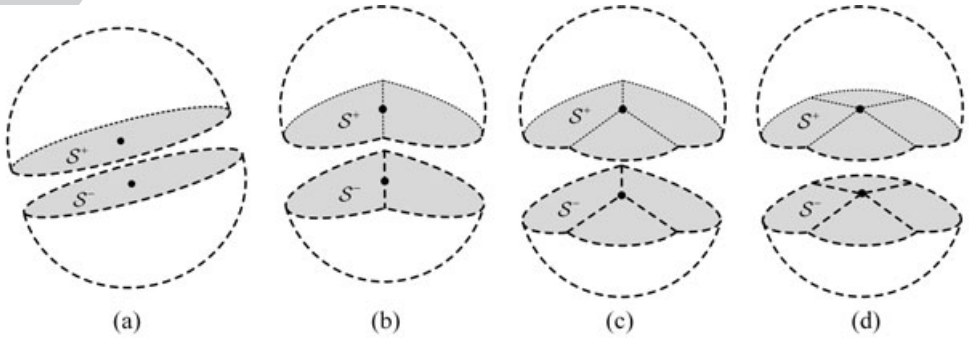

Figure 5. The support of cracking particles: (a) the original CPM; (b-d) proposed CPM with different segment numbers: 2, 3 and 4.

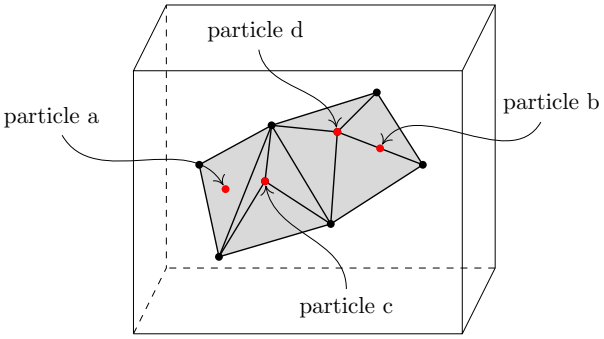

Figure 6. Crack surfaces presented by triangular meshes in a cube problem domain.

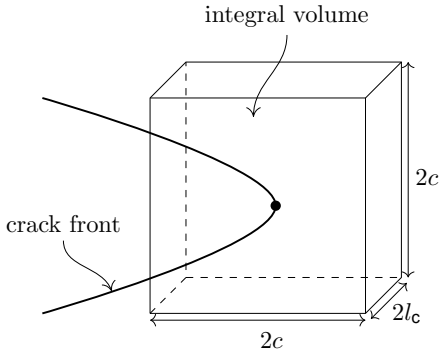

Figure 7. A volume for the interaction integral at a crack front particle.

integral. In this work, the interaction integral [59] is used to calculate SIFs. Two stress fields are required, namely the real state and an auxiliary state. The interaction integral at one crack front particle is evaluated as

$$I = \frac{1}{l_c}\int_V (\sigma_{ij}^{\text{aux}} u_{j,1} + \sigma_{ij} u_{j,1}^{\text{aux}} - \sigma_{jk}^{\text{aux}} \varepsilon_{jk} \delta_{1i}) q_{,i}\, \mathrm{d}V, \quad i,j,k \in \{1,2,3\}\,, \tag{7}$$

$$I = 2\frac{(1-\nu^2)}{E}(K_{\text{I}} K_{\text{I}}^{\text{aux}} + K_{\text{II}} K_{\text{II}}^{\text{aux}}) + \mu K_{\text{III}} K_{\text{III}}^{\text{aux}}, \tag{8}$$

where $q = (1 - \frac{|x|}{c})(1 - \frac{|y|}{c})(1 - \frac{|z|}{l_c})$ is a weight function, c and l_c are sizes of the volume as in Fig 7 and the superscript "aux" indicates the auxiliary state. The auxiliary field is predefined to obtain the three SIFs. For instance, if $K_{\text{I}}^{\text{aux}} = 1$, $K_{\text{II}}^{\text{aux}} = 0$ and $K_{\text{III}}^{\text{aux}} = 0$ then $I = 2\frac{(1-\nu^2)}{E} K_{\text{I}}$. The

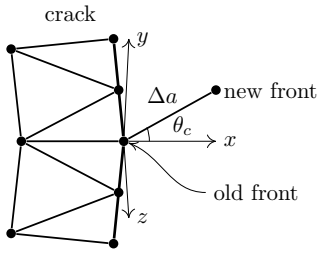

Figure 8. Local coordinates at crack fronts.

definition of auxiliary field can be found in many papers also using the interaction integral, e.g. [59, 60, 61]. This integration is calculated in a local coordinate system centred at the crack front particle and over a cube as in Fig 7. In [60], a curvilinear coordinate system is used for 3D cracks with curved and non-planar surfaces. Since flat triangular meshes are used here to model crack surfaces, integrating over a cube with a Cartesian coordinate system is appropriate and keeps the calculation simple [26, 9, 27, 62].

A local coordinate system as shown in Fig 8 is used,

$$\vec{x} = \frac{\sum_i^n \vec{l_i}}{\sum_i^n l_i}, \quad \vec{y} = \frac{\sum_i^n A_i \vec{n}_i}{\sum_i^n A_i}, \quad \vec{z} = \vec{x} \times \vec{y}, \tag{9}$$

where $\vec{x}$ is the extension vector of the crack front, $\vec{y}$ is the normal of the crack surface and $\vec{z}$ is the tangent of the crack front. l_i is the length of a line connected to the vertex and $\vec{l_i}$ is the vector. A_i is the area of a triangle connected to the vertex and $\vec{n}_i$ is the normal. Normally $\vec{x}$ and $\vec{y}$ are not orthogonal in Eq (9), and in that case then the projection of $\vec{y}$ on $\vec{x}$ needs to be removed and $\vec{y}$ is renormalized.

3.3. Crack propagation.

Crack propagation in 3D is modelled by determining the new positions of the crack front and connecting it to the old front with a triangular mesh. There are two parameters involved in advancing the fronts, increment angle and length, within the current algorithm. The crack propagating angle can be evaluated by a number of methods such as the maximum principal stress criterion, the minimum strain energy density criterion and the maximum strain energy release rate criterion (comparisons of all three are given in [63] for 2D cracks and in [64] for 3D). For simplicity, here it is assumed that mode III does not change the propagation angle and direction is set by the maximum principal stress criterion as in [27]. The increment angle θ_c in Fig 8 is determined with respect to the x axis in the xy plane under the local coordinate system, as

$$\theta_c = 2 \arctan \left(\frac{K_{\mathrm{I}} - \sqrt{K_{\mathrm{I}}^2 + 8K_{\mathrm{II}}^2}}{4K_{\mathrm{II}}} \right). \tag{10}$$

The incremental magnitude of movement of the crack front is here determined by the Paris' law [27], which describes the relationship between the crack extension $\mathrm{d}a$, the load cycle $\mathrm{d}N$ and the range of the stress intensity factor during the fatigue cycle ΔK_{eq} as

$$\frac{\mathrm{d}a}{\mathrm{d}N} = C(\Delta K_{\mathrm{eq}})^m, \tag{11}$$

where C and m are material constants and K_{eq} is the "equivalent" mode I stress intensity factor evaluated from the three stress intensity factors,

$$K_{\mathrm{eq}}^2 = \left(K_{\mathrm{I}} \cos^3 \frac{\theta_c}{2} - 3K_{\mathrm{II}} \cos^2 \frac{\theta_c}{2} \sin \frac{\theta_c}{2} \right)^2 + \frac{E}{(1-\nu^2)2\mu} K_{\mathrm{III}}^2. \tag{12}$$

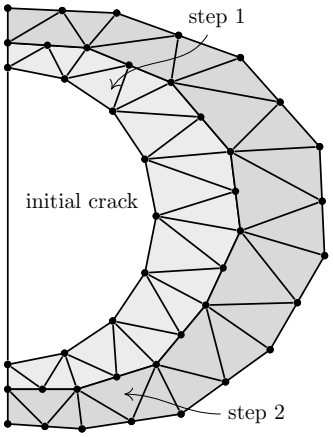

Figure 9. Crack propagation steps.

Although the Paris' law is originally for fatigue crack problems, it can provide a relationship between the crack incremental length and the value of the equivalent stress intensity factor and therefore can be applied here for a 3D crack under a quasi-static loading, e.g. examples [27, 29]. If the crack front particle with the maximum K_{eq} is set to a given length Δa_{max}, then the other front particles i are set incremental length following

$$\Delta a_i = \Delta a_{\text{max}} \left(\frac{\Delta K_{\text{eq}}}{\Delta K_{\text{eq}}^{\text{max}}} \right)^m. \tag{13}$$

After defining the increment length and angle, the location of the new front can be determined easily. Looping over all crack front particles, a particle is first advanced to a new location,

$$\mathbf{x}_i^{\text{new}} = \mathbf{x}_i + \Delta a_i Q^{-1} \cdot [\cos(\theta_c), \sin(\theta_c), 0]^{\text{T}}, \tag{14}$$

where $\mathbf{x}_i$ is the location of the front particle, $\mathbf{x}_i^{\text{new}}$ is the new position after crack propagation and Q is the rotation matrix from the global coordinates to the local coordinates. Either a new particle is created if there is no particle at the new location or the existing particle at the new location becomes cracked. Then the old and new crack front particles are connected by triangular meshes, and new crack surfaces are generated as in Fig 9. The two steps are repeated to achieve successive crack propagation steps, and the adaptivity mentioned above is carried out to handle the refinement of particles around the new front, which is described in an algorithm below.

4. EXAMPLES.

Several challenging numerical examples are presented to demonstrate the ability of the proposed methodology. The first is a penny-shaped crack in a cube under uniform tensile loading in one direction, and the calculated results are compared with theoretical solutions to check the accuracy. In the second example, the boundary conditions are the same as the first but the crack is rotated producing a mixed mode crack problem, and in addition in this example, the crack is then propagated. The final example is a lens-shaped crack problem which is a test of the abilities of the method to model curved crack surfaces. All three examples are in a cube domain of side length $2w = 200$mm. A regular distribution of $15 \times 15 \times 15$ particles is set initially from which adaptive refinement proceeds. Volume integration is performed using $14 \times 14 \times 14$ cells with arrangements of $4 \times 4 \times 4$ Gauss points. Integration on surfaces where external loadings are applied is performed using 14×14 cells each with 8×8 Gauss points. The motion and rotation of the cube are locked by Eqs (15) and (16) respectively based on the conservation of momentum, and essential boundary

Algorithm 1 Crack propagation for a 3D crack

```
Achieve SIFs of all front particles by Eqs (7, 8)
Determine incremental angle θ_c by Eq (10)
Calculate equivalent SIF by Eq (12)
Find the maximum K_eq
for i=1:n_c % loop over all crack front particles do
    Set incremental magnitude Δa_I by Eq (13)
    Obtain the position of the new front by Eq (14)
    if there is no particle at the new position then
        Create new cracking particle
    else
        The particle at the new position becomes cracked
    end if
end for
Update the information of old front particles
Create new triangular meshes connecting old and new front particles
```

conditions are imposed with Lagrange multipliers.

$$\int_V u_x \mathrm{d}V = 0, \int_V u_y \mathrm{d}V = 0, \int_V u_z \mathrm{d}V = 0. \tag{15}$$

$$\int_V \frac{\partial u_x}{\partial y} - \frac{\partial u_y}{\partial x} \mathrm{d}V = 0, \int_V \frac{\partial u_x}{\partial z} - \frac{\partial u_z}{\partial x} \mathrm{d}V = 0, \int_V \frac{\partial u_y}{\partial z} - \frac{\partial u_z}{\partial y} \mathrm{d}V = 0. \tag{16}$$

The approach here to impose essential boundary conditions is uniform and applicable for both symmetrical and asymmetrical problems. This approach can provide exactly symmetrical results for the example 1 and makes implementation of the boundary conditions for examples 2 and 3 much easier and more accurate than by fixing some faces of the cube as in [29]. The calculation of these integrations is not a burden since it can be obtained in the process of assembling the system stiffness matrix, and only six Lagrange multipliers are required. The constant in the crack propagation Eq (13) used in all analyses is $m = 3.32$ from [27]. The error of SIFs along a crack front in all three examples is given by

$$e_{F_n} = \frac{\sum_k^{n_c} |F_n^k - F_n^0|}{n_c F_n^0}, \quad n \in \{\text{I, II, III}\} \tag{17}$$

where n_c is the number of crack front nodes, F_n are normalized SIFs defined later and F_n^0 are the exact values.

4.1. A penny-shaped crack.

The penny-shaped crack problem is a mode I crack problem. The problem is shown in Fig 10 where the radius of the crack is $a = w/10$, and elastic material is assumed with $E = 100$GPa and $\nu = 0.3$. The upper and lower faces of the cube are subject to normal stresses producing uniaxial tension $\sigma = 100\text{N/m}^2$, and the target global error is set to be $\eta = 0.008$. Since the crack face is a circle, no triangular mesh is used here and the circle itself is employed directly for checking the visibility among particles. The theoretical solutions for the mode I SIF and the crack opening shapes are given by Eqs (18) and (19) [65]. For the purposes of results presentation, the K_I SIF is normalized to $F_\mathrm{I} = \frac{K_\mathrm{I}}{2\sigma}\sqrt{\pi/a}$.

$$u = \frac{4(1-\nu^2)}{\pi E}\sigma\sqrt{a^2 - r^2}, \tag{18}$$

$$K_\mathrm{I} = \frac{2}{\pi}\sigma\sqrt{\pi a}. \tag{19}$$

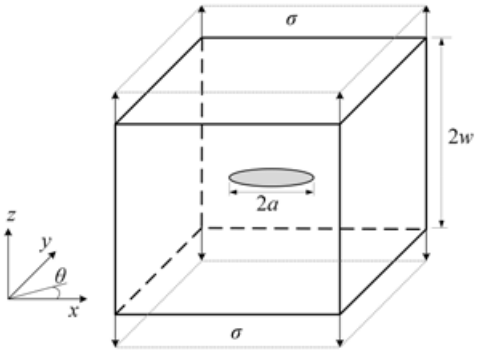

Figure 10. A penny-shaped crack in a cube, subjected to uniform tensile stress.

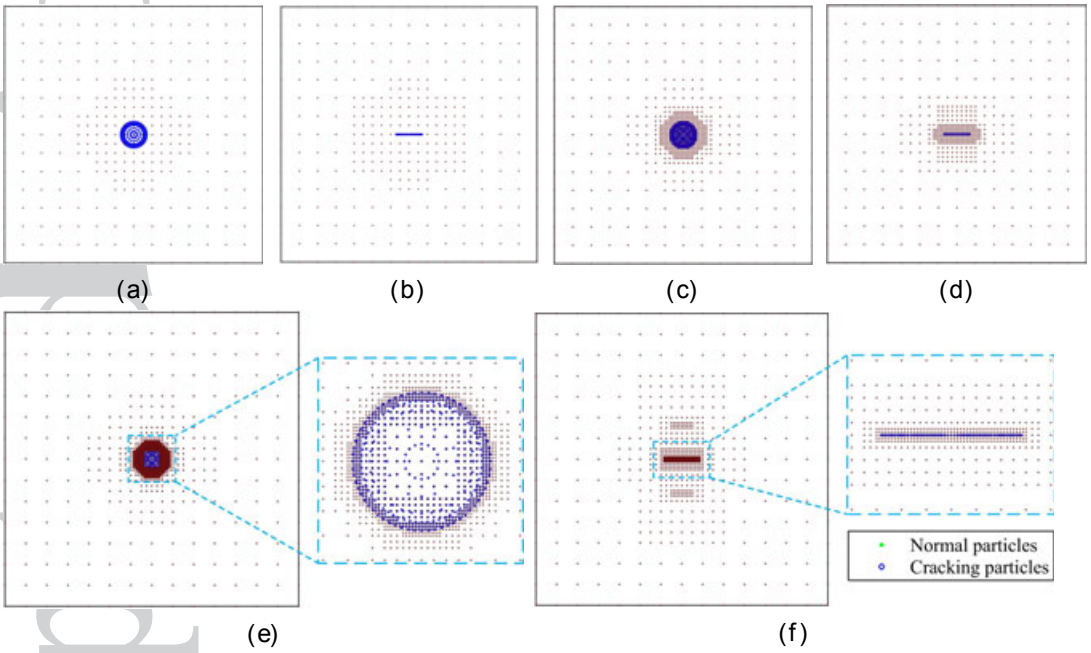

Figure 11. Node arrangements during adaptive steps of the penny-shaped crack problem: (a) xy view for step 1; (b) xz view for step 1; (c) xy view for step 3; (d) xz view for step 3; (e) xy view for step 5; (f) xz view for step 5.

Nodal arrangements are adjusted by the adaptive approach described above and particles are added around the crack front as shown in Fig 11. The convergence rate of error reduction of these adaptive steps is higher than by uniform refinement as shown in Fig 12 (a). More accurate SIFs can be obtained using the adaptive approach with the same number of particles. From the convergence rates, it can be seen that uniform refinement over the cube is unpractical since the crack is much smaller than the cube. The final deformation of the crack is shown in Fig 13 and the elliptical crack opening shape in the xz view is clear in Fig 13 (b). The crack opening shape and mode I SIF are shown in Fig 14, where θ is the angle from a crack front to the x axis in the xy plane seen in Fig 10 and r is the distance to the circle centre. In Fig 14 (a), the displacements of cracking particles are seen to match well with analytical solutions in four different directions. With an adaptivity approach, the accuracy along the curved crack front is maintained even with uniformly distributed particles. Calculated SIFs also agree with the analytical solutions as indicated in Fig 14 (b).

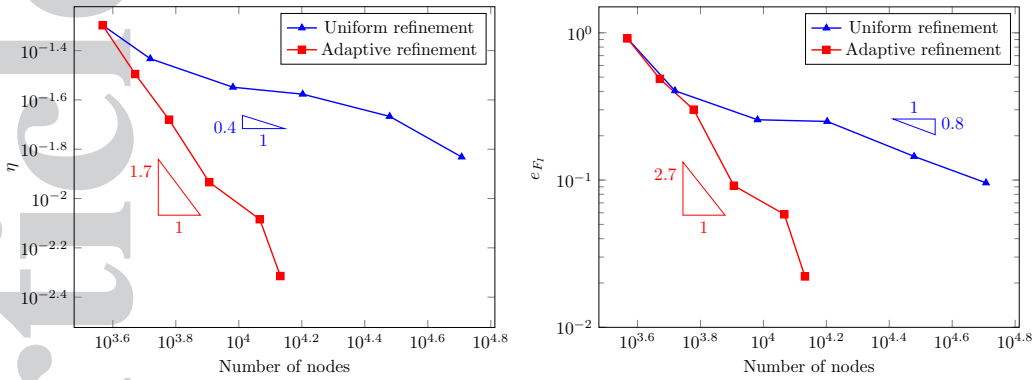

Figure 12. Adaptive steps of a penny-shaped crack problem: (a) convergent rate; (b) normalized K_{I}.

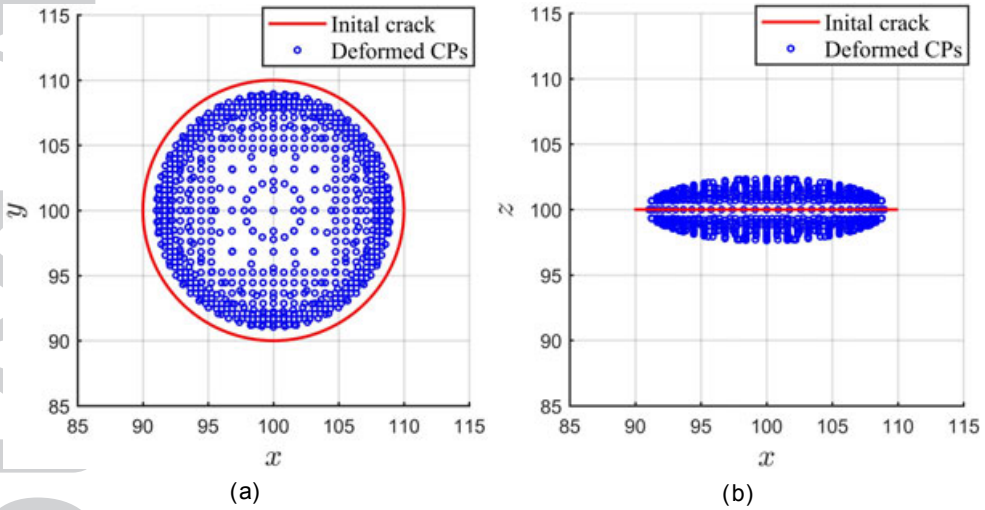

Figure 13. Deformation (unit mm) multiplied by 200 times of a penny-shaped crack under uniaxial tensile loading: (a) xy view; (b) xz view.

4.2. An inclined penny-shaped crack.

If the penny-shaped crack of the first example is rotated while the other aspects of the problem are fixed, then the problem becomes one of mixed-mode fracture. This problem is shown in Fig 15, where a larger crack radius $a = w/5$ is set and the rotation angle is given as $\beta = \pi/6$ in the xz plane to the x axis. Material properties and boundary conditions are the same as the first example. Again the circle itself is used to define connectivity between particles, while a triangular mesh is used to describe crack geometries after crack propagation. The target global error is set a little higher to $\eta = 0.02$, since it is hard to pursue a high accuracy after the crack propagates to a complicated surface.

The deformation of the initial crack is in shown Fig 16, showing that the crack rotates by a small angle relative to the original location. Stress intensity factors along the crack front are calculated and compared (with analytical solutions in Eqs (20-22) from [65]). In Fig 17, θ is defined the same as the first example. Although a regular distribution of nodes is used, similar results are obtained along the curved crack front. There are, however, two points at which numerical results vary from the analytical solutions noticeably: at $\theta = 0$ and $\theta = \pi$ due to boundary effects. Similar issues can be found in the results presented in [30]. It can be seen that $K_{\mathrm{III}} = 0$ at $\theta = 0$ where the deformation is predominantly mode I and II , while $K_{\mathrm{II}} = 0$ at $\theta = \pi/2$ where the deformation is predominantly

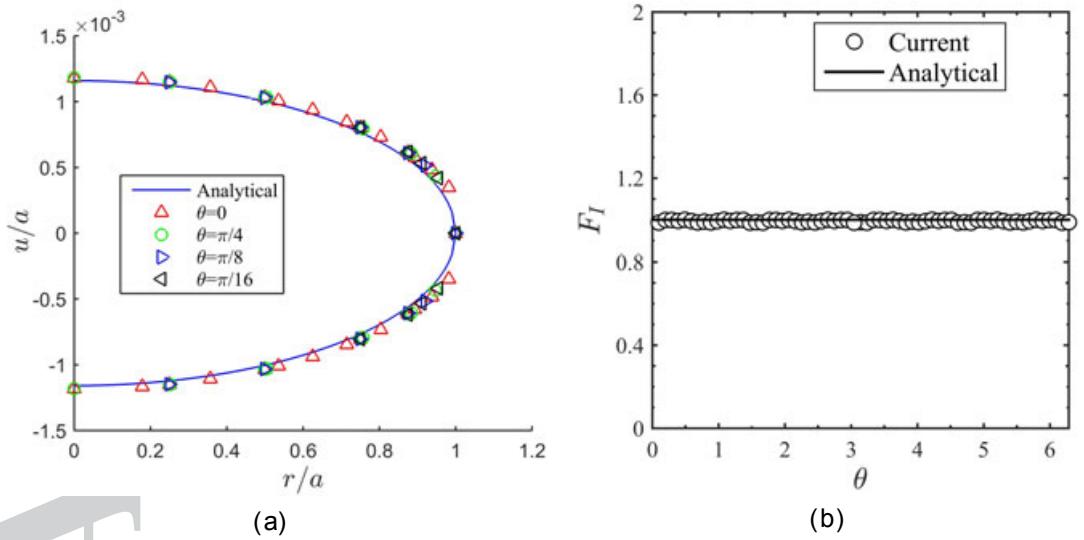

Figure 14. Verification of the current method by analytical results: (a) crack opening shape; (b) normalized K_{I}

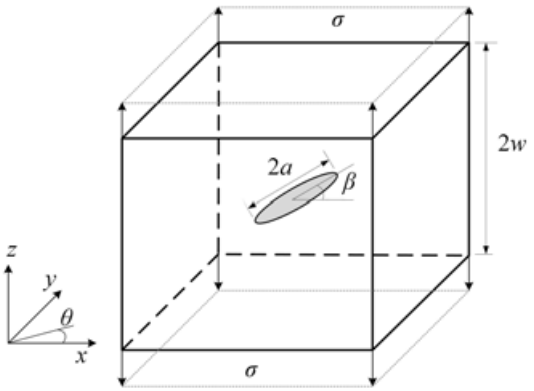

Figure 15. Example problem 2: An inclined penny-shaped crack inside a cubic domain under uniaxial tensile loading.

mode I and III. Crack propagation for this problem is shown in Fig 18 where new crack surfaces are described by a triangular mesh, as described above. There two "kinks", at $\theta = \pi/2$ and $\theta = 3\pi/2$, which are caused by mode III fracture, which is consistent with the deformation pattern.

$$K_{\mathrm{I}} = 2\sigma \cos^2 \beta \sqrt{\frac{a}{\pi}}. \tag{20}$$

$$K_{\mathrm{II}} = -\frac{4\sigma}{2-\nu} \sin\beta \cos\beta \sqrt{\frac{a}{\pi}} \cos\theta. \tag{21}$$

$$K_{\mathrm{III}} = -\frac{4(1-\nu)\sigma}{2-\nu} \sin\beta \cos\beta \sqrt{\frac{a}{\pi}} \sin\theta. \tag{22}$$

4.3. A lens-shaped crack.

In the final example, a lens-shaped crack with curved crack surfaces in a cube-shaped domain as shown in Fig 19 is considered. The geometry of the crack is given by $r = w/5$, $\beta = \pi/4$, and

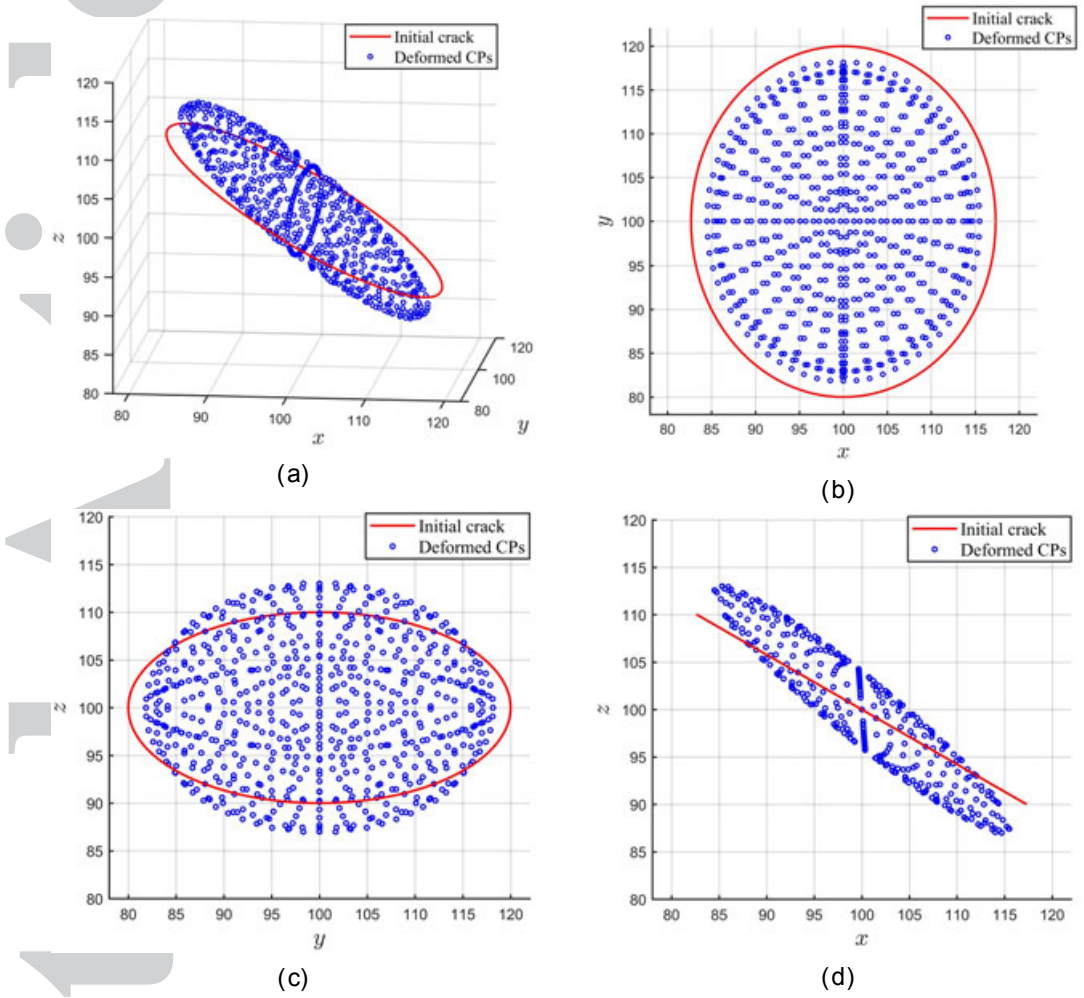

Figure 16. Deformation (unit mm) multiplied by 200 times of an inclined penny-shaped crack under uniaxial tensile loading: (a) xyz view; (b) xy view; (c) yz view; (d) xz view.

material properties used are $E = 68.9$GPa and $\nu = 0.22$ the same as the values in [60]. The six faces of the cube are under tensile loading $\sigma = 100$N/m^2. The SIFs, K_n are normalized as

$$F_n = \frac{K_n}{2\sigma}\sqrt{\frac{\pi}{r\sin\beta}}, \tag{23}$$

where $n =$ I, II or III. The results are compared with values $F_{\mathrm{I}} = 0.874$, $F_{\mathrm{II}} = 0.225$ and $F_{\mathrm{III}} = 0$ from [60].

A comparison between the original CPM and the proposed method is now presented. In the following calculations, the default particle arrangements are used and some refinements of particles around the crack are predefined. The crack is described by the overlap of planar discontinuous segments in the original CPM in Fig 20 (a) and is also modelled by a triangular mesh in the new method in Fig 20 (b). Checking a "slice" view at $y = 100$mm in Fig 20 (c), it can be seen that crack modelling by the original CPM is discontinuous while the proposed method is continuous. In the original CPM, there is a requirement to shift integration points which are invisible to other particles due to the discontinuous segments, but this is not necessary for the proposed method. Fig 21 (a) shows that the global errors using the proposed method are much lower than those calculated by the original CPM, but the difference reduces when finer particle distributions are used. It follows that the calculation of SIFs by the proposed method is more accurate as shown in Fig 21 (b-c). For coarse

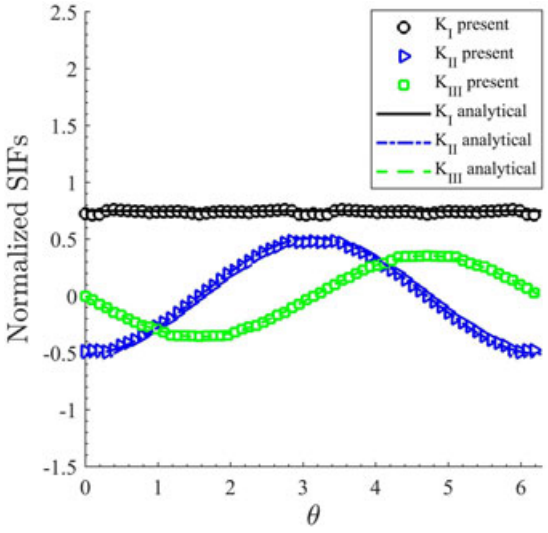

Figure 17. SIFs along the crack front for the inclined penny-shaped crack problem.

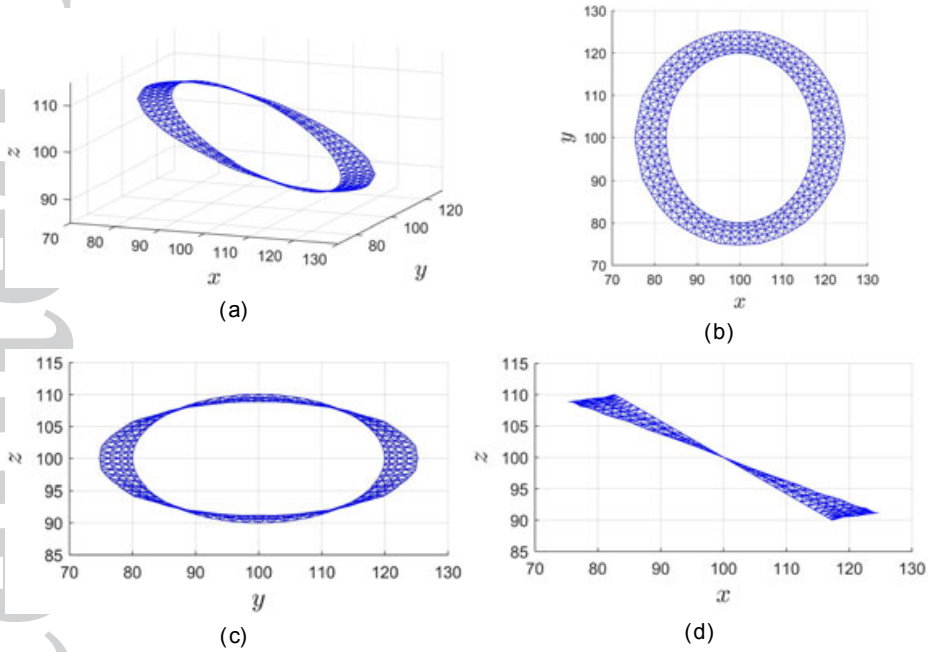

Figure 18. Crack propagation (unit mm) of an incline penny-shaped crack under uniaxial tensile: (a) xyz view; (b) xy view; (c) yz view; (d) xz view.

arrangements of particles, both methods provide similar results for K_{I}, but when fine refinement takes place and more information around crack surfaces is collected, the proposed method shows better accuracy than the original CPM, Fig 21 (b). The deformation of the crack by the proposed CPM is shown in Fig 22, and a slice view at $y = 100$mm is shown in Fig 22 (c) to illustrate the crack opening. SIFs along the crack front by the proposed method are given in Fig 23, where good agreement with the reference values is obtained. Both the proposed and the original CPM can reach a good accuracy when a fine particle distribution is used. The advantage of the proposed method over the original is the ability to align the crack segments so that a better description of crack geometries is obtained, especially for applications to model cracks with high curvatures.

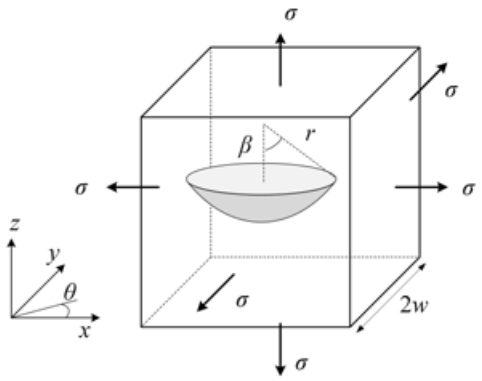

Figure 19. Example problem 3: A lens-shaped crack in a cube under hydrostatic tensile loading.

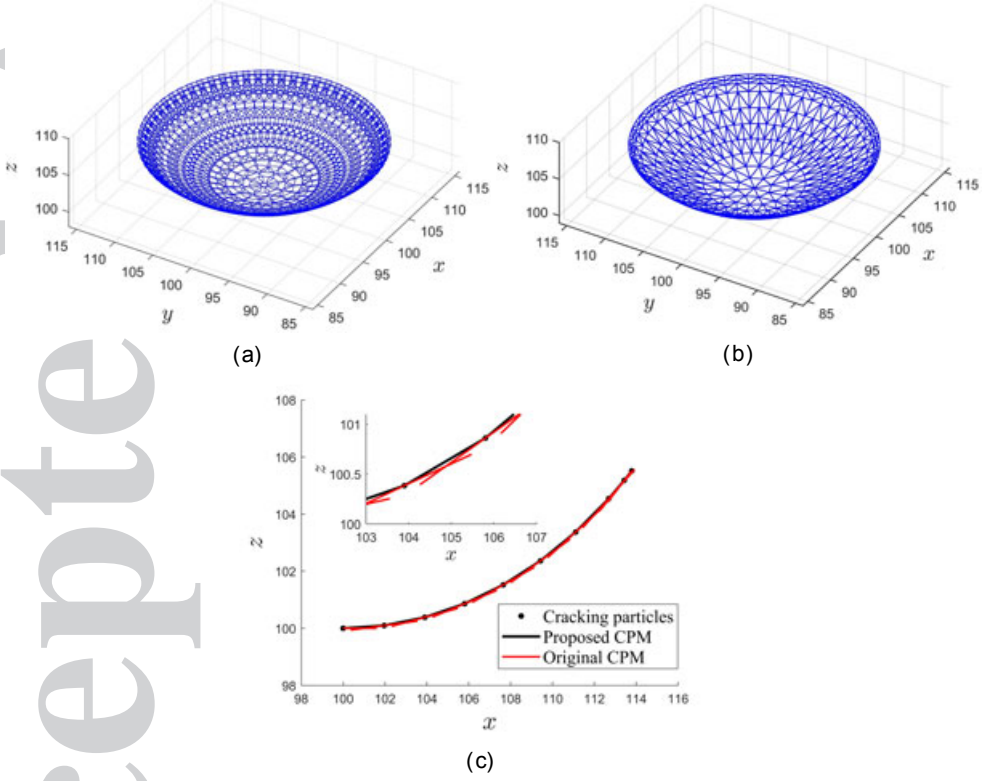

Figure 20. Comparison of crack surface description between the original CPM and the proposed CPM: (a) original CPM; (b) proposed CPM; (c) slice view at $y = 100$ (unit mm).

5. SUMMARY.

A framework for 3D fracture modelling with an explicit description for 3D cracks has been proposed. The methodology is based on the CPM, where 3D crack surfaces are represented by a set of discontinuous segments located by cracking particles. Particles on crack surfaces are assumed ot be split into two parts. Supports of particles are modified by those segments and then discontinuities of cracks are introduced with the use of the visibility criterion. The geometries of crack surfaces during crack propagation steps are recorded by triangular meshes built from original crack fronts and the orientations of discontinuous segments are adjusted according to the angular change of crack propagation. For those particles inside a triangular element, the supports are the same as the original

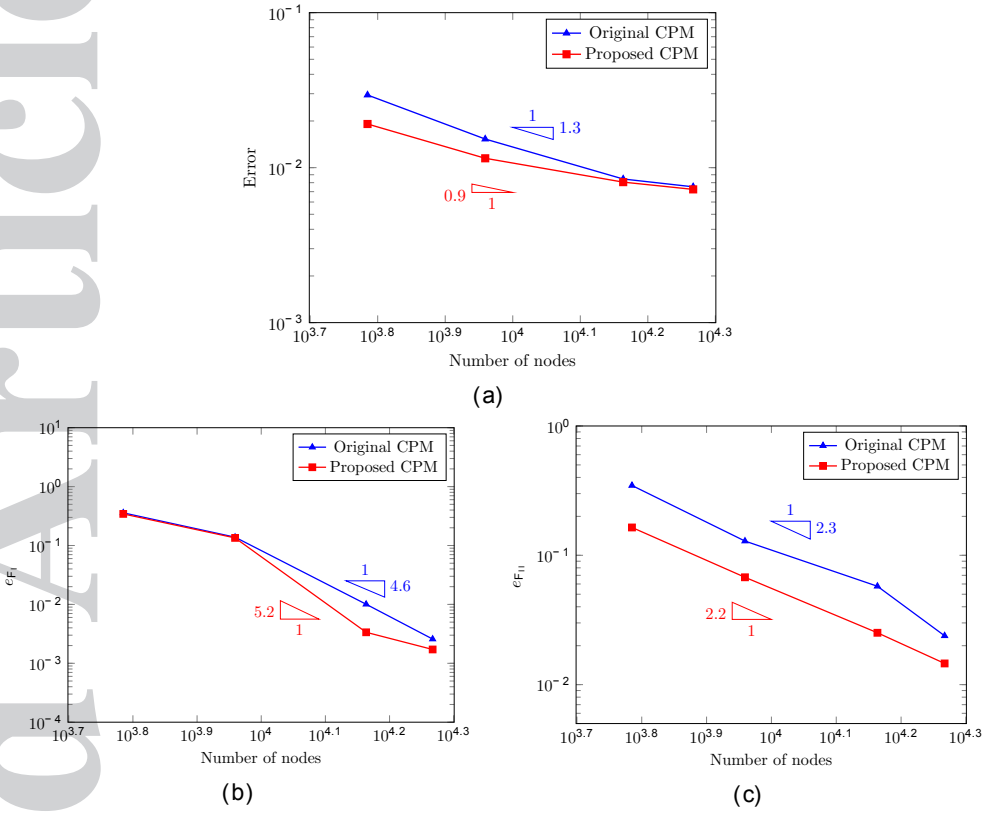

Figure 21. Comparison of results between the original CPM and the proposed CPM: (a) global error; (b) F_{I} at dashed line; (c) F_{II} at dashed line.

CPM, while for the others on the edges of triangles, the supports are adjusted by the use of non-planar segments. An adaptive approach in 3D has been introduced to capture the stress gradients at crack fronts. The original and proposed methodologies are compared using a lens-shaped crack problem, and the proposed method shows a higher error convergence rate with more accurate results for SIFs.

ACKNOWLEDGEMENT

The authors acknowledge the support from the China Scholarship Council (CSC) and the Faculty of Science, Durham University.

REFERENCES

1. Nguyen VP, Rabczuk T, Bordas S, Duflot M. Meshless methods: a review and computer implementation aspects. *Mathematics and Computers in Simulation.* 2008;79(3):763–813.
2. Chen JS, Hillman M, Chi S. Meshfree Methods: Progress Made after 20 Years. *Journal of Engineering Mechanics.* 2017;143(4):04017001.
3. Schöllmann M, Fulland M, Richard H. Development of a new software for adaptive crack growth simulations in 3D structures. *Engineering Fracture Mechanics.* 2003;70(2):249–268.
4. Belytschko T, Black T. Elastic crack growth in finite elements with minimal remeshing. *International Journal for Numerical Methods in Engineering.* 1999;45(5):601–620.
5. Daux C, Moes N, Dolbow J, Sukumar N, Belytschko T. Arbitrary branched and intersecting cracks with the extended finite element method. *International Journal for Numerical Methods in Engineering.* 2000;48:1741–1760.
6. Belytschko T, Moës N, Usui S, Parimi C. Arbitrary discontinuities in finite elements. *International Journal for Numerical Methods in Engineering.* 2001;50(4):993–1013.
7. Budyn E, Zi G, Moës N, Belytschko T. A method for multiple crack growth in brittle materials without remeshing. *International Journal for Numerical Methods in Engineering.* 2004;61(10):1741–1770.

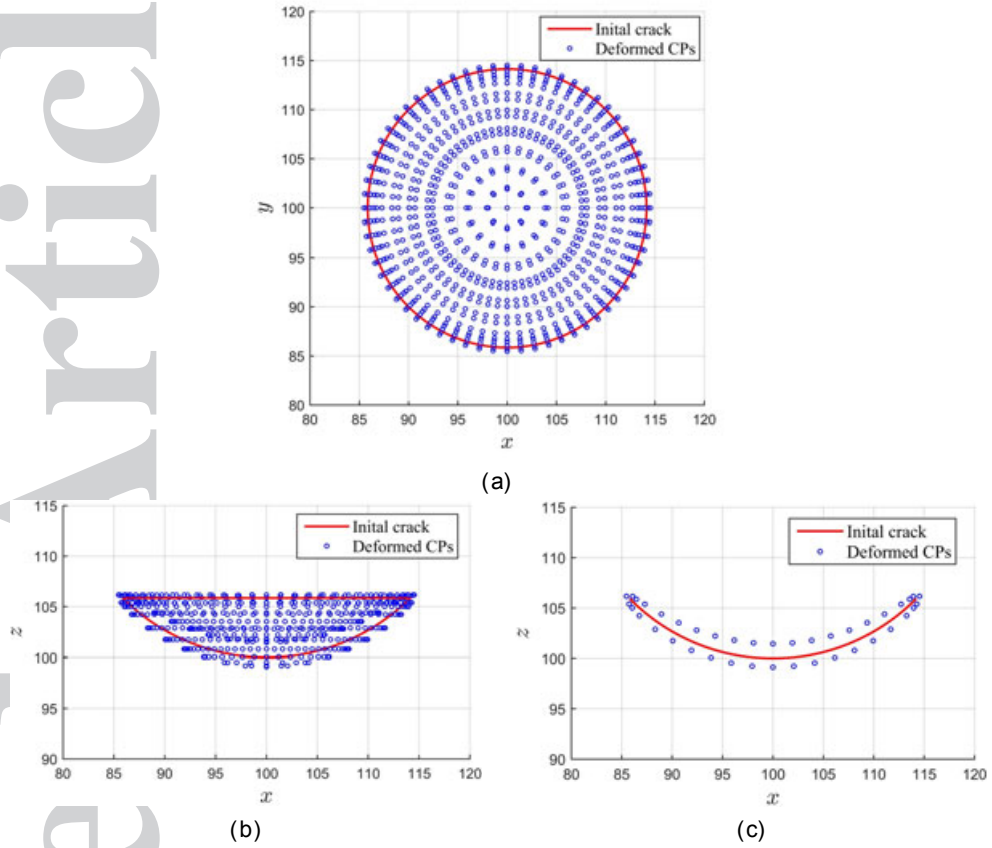

Figure 22. Deformation multiplied by 50 times of a lens-shaped crack under quadratic tensile loading: (a) xy view; (b) xz view; (c) slice view at $y = 100$ (unit mm).

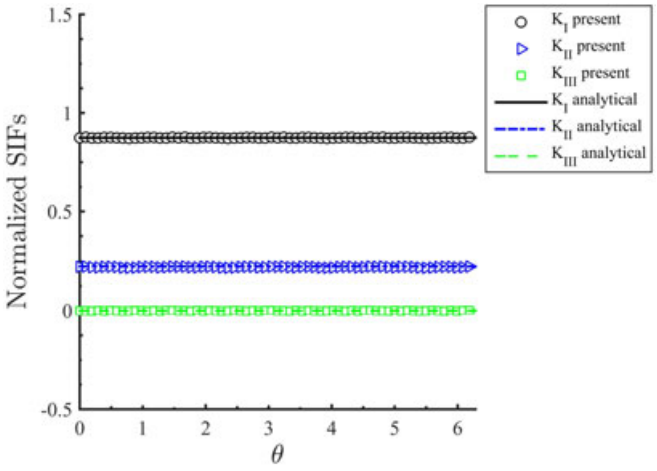

Figure 23. SIFs along the crack front of a lens-shaped crack.

8. Sukumar N, Moës N, Moran B, Belytschko T. Extended finite element method for three-dimensional crack modelling. *International Journal for Numerical Methods in Engineering.* 2000;48(11):1549–1570.
9. Moës N, Gravouil A, Belytschko T. Non-planar 3D crack growth by the extended finite element and level sets - Part I: Mechanical model. *International Journal for Numerical Methods in Engineering.* 2002;53(11):2549–2568.
10. Gravouil A, Moës N, Belytschko T. Non-planar 3D crack growth by the extended finite element and level sets - Part II: Level set update. *International Journal for Numerical Methods in Engineering.* 2002;53(11):2569–2586.

11. Duflot M. A study of the representation of cracks with level sets. *International Journal for Numerical Methods in Engineering.* 2007;70(11):1261–1302.
12. Fries TP, Baydoun M. Crack propagation with the extended finite element method and a hybrid explicit–implicit crack description. *International Journal for Numerical Methods in Engineering.* 2012;89(12):1527–1558.
13. Ma G, An X, Zhang H, Li L. Modeling complex crack problems using the numerical manifold method. *International Journal of Fracture.* 2009;156(1):21–35.
14. Zhang H, Li L, An X, Ma G. Numerical analysis of 2-D crack propagation problems using the numerical manifold method. *Engineering Analysis with Boundary Elements.* 2010;34(1):41–50.
15. Shi GH. Discontinuous deformation analysis: a new numerical model for the statics and dynamics of deformable block structures. *Engineering Computations.* 1992;9(2):157–168.
16. Yang Y, Tang X, Zheng H, Liu Q, He L. Three-dimensional fracture propagation with numerical manifold method. *Engineering Analysis with Boundary Elements.* 2016;72:65–77.
17. Cai Y, Wu J, Atluri S. A new implementation of the numerical manifold method (NMM) for the modeling of non-collinear and intersecting cracks. *Computer Modeling in Engineering & Sciences.* 2013;92(1):63–85.
18. Belytschko T, Lu Y, Gu L. Element-free Galerkin methods. *International Journal for Numerical Methods in Engineering.* 1994;37(2):229–256.
19. Belytschko T, Gu L, Lu Y. Fracture and crack growth by element free Galerkin methods. *Modelling and Simulation in Materials Science and Engineering.* 1994;2(3A):519–534.
20. Belytschko T, Lu Y, Gu L. Crack propagation by element-free Galerkin methods. *Engineering Fracture Mechanics.* 1995;51(2):295–315.
21. Zhuang X, Augarde C, Bordas S. Accurate fracture modelling using meshless methods, the visibility criterion and level sets: formulation and 2D modelling. *International Journal for Numerical Methods in Engineering.* 2011;86(2):249–268.
22. Belytschko T, Lu Y, Gu L, Tabbara M. Element-free Galerkin methods for static and dynamic fracture. *International Journal of Solids and Structures.* 1995;32(17):2547–2570.
23. Lu Y, Belytschko T, Tabbara M. Element-free Galerkin method for wave propagation and dynamic fracture. *Computer Methods in Applied Mechanics and Engineering.* 1995;126(1-2):131–153.
24. Belytschko T, Organ D, Gerlach C. Element-free Galerkin methods for dynamic fracture in concrete. *Computer Methods in Applied Mechanics and Engineering.* 2000;187(3-4):385–399.
25. Sukumar N, Moran B, Black T, Belytschko T. An element-free Galerkin method for three-dimensional fracture mechanics. *Computational Mechanics.* 1997;20(1):170–175.
26. Krysl P, Belytschko T. The Element Free Galerkin method for dynamic propagation of arbitrary 3-D cracks. *International Journal for Numerical Methods in Engineering.* 1999;44(6):767–800.
27. Duflot M. A meshless method with enriched weight functions for three-dimensional crack propagation. *International Journal for Numerical Methods in Engineering.* 2006;65(12):1970–2006.
28. Bordas S, Rabczuk T, Zi G. Three-dimensional crack initiation, propagation, branching and junction in non-linear materials by an extended meshfree method without asymptotic enrichment. *Engineering Fracture Mechanics.* 2008;75(5):943–960.
29. Zhuang X, Augarde C, Mathisen K. Fracture modeling using meshless methods and level sets in 3D: framework and modeling. *International Journal for Numerical Methods in Engineering.* 2012;92(11):969–998.
30. Barbieri E, Petrinic N. Three-dimensional crack propagation with distance-based discontinuous kernels in meshfree methods. *Computational Mechanics.* 2014;53(2):325–342.
31. Silling SA, Askari E. A meshfree method based on the peridynamic model of solid mechanics. *Computers & Structures.* 2005;83(17):1526–1535.
32. Ha YD, Bobaru F. Studies of dynamic crack propagation and crack branching with peridynamics. *International Journal of Fracture.* 2010;162(1):229–244.
33. Ren B, Wu C, Askari E. A 3D discontinuous Galerkin finite element method with the bond-based peridynamics model for dynamic brittle failure analysis. *International Journal of Impact Engineering.* 2017;99:14–25.
34. Rabczuk T, Belytschko T. Cracking particles: a simplified meshfree method for arbitrary evolving cracks. *International Journal for Numerical Methods in Engineering.* 2004;61(13):2316–2343.
35. Rabczuk T, Belytschko T. Application of particle methods to static fracture of reinforced concrete structures. *International Journal of Fracture.* 2006;137(1-4):19–49.
36. Rabczuk T, Song J, Belytschko T. Simulations of instability in dynamic fracture by the cracking particles method. *Engineering Fracture Mechanics.* 2009;76(6):730–741.
37. Kumar V, Drathi R. A meshless cracking particles approach for ductile fracture. *KSCE Journal of Civil Engineering.* 2014;18(1):238-248.
38. Kumar V, Ghosh A. Non-linear dynamic fragmentation using Cracking Particles Method. *Computation Materials Science.* 2015;98:117–122.
39. Rabczuk T, Belytschko T. A three-dimensional large deformation meshfree method for arbitrary evolving cracks. *Computer Methods in Applied Mechanics and Engineering.* 2007;196(29):2777–2799.
40. Rabczuk T, Zi G, Bordas S, Nguyen-Xuan H. A simple and robust three-dimensional cracking-particle method without enrichment. *Computer Methods in Applied Mechanics and Engineering.* 2010;199(37):2437–2455.
41. Xu S. Stable cracking particles method based on stabilized nodal integration and updated Lagrangian kernel. *Mathematical Problems in Engineering.* 2014;article-ID 646514:1-10.
42. Ai W, Augarde CE. An adaptive cracking particle method for 2D crack propagation. *International Journal for Numerical Methods in Engineering.* 2016;108(13):1626–1648.
43. Sanders O. Cohesive cracking using the cracking particle method. Master's thesis, Department of Engineering, Durham University, UK. 2017.
44. Lu Y, Belytschko T, Gu L. A new implementation of the element free Galerkin method. *Computer Methods in Applied Mechanics and Engineering.* 1994;113(3):397–414.

45. Dolbow J, Belytschko T. A finite element method for crack growth without remeshing. *International Journal for Numerical Methods in Engineering.* 1999;46(1):131–150.
46. Organ D, Fleming M, Terry T, Belytschko T. Continuous meshless approximations for nonconvex bodies by diffraction and transparency. *Computational Mechanics.* 1996;18(3):225–235.
47. Chung H, Belytschko T. An error estimate in the EFG method. *Computational Mechanics.* 1998;21(2):91–100.
48. Lee CK, Zhou C. On error estimation and adaptive refinement for element free Galerkin method: Part I: stress recovery and a posteriori error estimation. *Computers & Structures.* 2004;82(4):413–428.
49. Rossi R, Alves MK. An h-adaptive modified element-free Galerkin method. *European Journal of Mechanics-A/Solids.* 2005;24(5):782–799.
50. Ullah Z, Augarde C. Finite deformation elasto-plastic modelling using an adaptive meshless method. *Computers & Structures.* 2013;118:39–52.
51. Le CV, Askes H, Gilbert M. Adaptive element-free Galerkin method applied to the limit analysis of plates. *Computer Methods in Applied Mechanics and Engineering.* 2010;199(37):2487–2496.
52. Rabczuk T, Belytschko T. Adaptivity for structured meshfree particle methods in 2D and 3D. *International Journal for Numerical Methods in Engineering.* 2005;63(11):1559–1582.
53. Ullah Z, Coombs W, Augarde C. An adaptive finite element/meshless coupled method based on local maximum entropy shape functions for linear and nonlinear problems. *Computer Methods in Applied Mechanics and Engineering.* 2013;267:111–132.
54. Ren H, Zhuang X, Cai Y, Rabczuk T. Dual-horizon peridynamics. *International Journal for Numerical Methods in Engineering.* 2016;108(12):1451–1476.
55. Ren H, Zhuang X, Rabczuk T. Dual-horizon peridynamics: A stable solution to varying horizons. *Computer Methods in Applied Mechanics and Engineering.* 2017;318:762–782.
56. Ai W, Augarde CE. A multi-cracked particle method for complex fracture problems in 2D. *Mathematics and Computers in Simulation.* under review;.
57. Rice JR. A path independent integral and the approximate analysis of strain concentration by notches and cracks. *Journal of Applied Mechanics.* 1968;35(2):379–386.
58. Brighenti R. Application of the element-free Galerkin meshless method to 3-D fracture mechanics problems. *Engineering Fracture Mechanics.* 2005;72(18):2808–2820.
59. Yau J, Wang S, Corten H. A mixed-mode crack analysis of isotropic solids using conservation laws of elasticity. *Journal of Applied Mechanics.* 1980;47(2):335–341.
60. Gosz M, Moran B. An interaction energy integral method for computation of mixed-mode stress intensity factors along non-planar crack fronts in three dimensions. *Engineering Fracture Mechanics.* 2002;69(3):299–319.
61. Yu H, Wu L, Guo L, Du S, He Q. Investigation of mixed-mode stress intensity factors for nonhomogeneous materials using an interaction integral method. *International Journal of Solids and Structures.* 2009;46(20):3710–3724.
62. Hu Y, Yang Z. An element-free Galerkin method for 3D crack propagation simulation under complicated stress conditions. *International Journal for Numerical Methods in Engineering.* 2012;91(12):1251–1263.
63. Bouchard PO, Bay F, Chastel Y. Numerical modelling of crack propagation: automatic remeshing and comparison of different criteria. *Computer Methods in Applied Mechanics and Engineering.* 2003;192(35):3887–3908.
64. Richard H, Fulland M, Sander M. Theoretical crack path prediction. *Fatigue & fracture of engineering materials & structures.* 2005;28(1-2):3–12.
65. Tada H, Paris P, Irwin G. The analysis of cracks handbook. *New York: ASME Press.* 2000;.